

Construction of Core-shell $\text{TiNb}_2\text{O}_7/\text{Li}_4\text{Ti}_5\text{O}_{12}$ Composites with Improved Lithium Storage for Lithium-Ion Batteries

Yu-Sheng Hsiao ^a, Lin-Yang Weng ^a, Ta-Hung Cheng ^{a, g}, Tzu-Yen Huang ^b, Yen-Ju Wu ^h, Jen-Hsien Huang ^c, Nian-Jheng Wu ^d, Shih-Chieh Hsu ^{e, *}, Huei Chu Weng ^{f, *}, Chih-Ping Chen ^{g, *}

^aDepartment of Materials Science and Engineering, National Taiwan University of Science and Technology, No. 43, Sec. 4, Keelung Road, Da-an District, Taipei, 10607, Taiwan

^bNational Synchrotron Radiation Research Center, 101 Hsin-Ann Road, Hsinchu Science Park, Hsinchu 30076, Taiwan

^cDepartment of Green Material Technology, Green Technology Research Institute, CPC Corporation, No.2, Zuonan Rd., Nanzi District, Kaohsiung City, 81126, Taiwan

^dUniversité Paris-Saclay, CNRS, Institut des Sciences Moléculaires d'Orsay, 91405 Orsay, France

^eDepartment of Chemical and Materials Engineering, Tamkang University, No. 151, Yingzhuan Road, Tamsui District, New Taipei City, 25137, Taiwan

^fDepartment of Mechanical Engineering, Chung Yuan Christian University, No. 200, Chungpei Rd, Chungli District, Taoyuan City 32023, Taiwan

^gDepartment of Materials Engineering, Ming Chi University of Technology, 84 Gungjuan Rd., Taishan District, New Taipei City, 24301, Taiwan

^hCenter for Basic Research on Materials, National Institute for Materials Science (NIMS), 1-2-1 Sengen, Tsukuba, Ibaraki 305-0047, Japan

^{e,*}Corresponding author. E-mail: 137422@o365.tku.edu.tw (S.-C. Hsu) Tel: +886-2-26215656#2032

^{f,*}Corresponding author. E-mail: hcweng@cycu.edu.tw (H. C. Weng) Tel.: +886-3-2654311

^{g,*}Corresponding author. E-mail: cpchen@mail.mcut.edu.tw (C.-P. Chen). Tel.: +886-2-29089899#4439

In this study, the (TiNb₂O₇) TNO and modified (Li₄Ti₅O₁₂) LTO composites with the core-shell (CS) structures have been designed and prepared by the spray-dried method. In the structural composite, the modified LTO core can stabilize the dimensional stability with excellent rate capability, and the TNO shell can offer a larger capacity, leading to high-performance anode materials. Our results indicate that the CS composites without the TNO nanoparticles (NPs) aggregation reveal a more negligible electrochemical polarization (EP) with improved kinetics than traditional composites. The optimal TNO content in the CS composite is 30 wt%, which can show a larger capacity than that of bare LTO, with the C-rate ranging between 17.5 and 3500 mA g⁻¹. It delivers a capacity of 164.9 mA h g⁻¹ at 1050 mA g⁻¹, higher than bare LTO (157.6 mA h g⁻¹) and traditional composite (154.6 mA h g⁻¹). Furthermore, the full lithium-ion battery (LIB) is fabricated using the CS composite as the anode and LiNi_{0.5}Mn_{1.5}O₄ (LNMO) as the cathode. The designed LIB shows an improved energy density of 122.0 W h kg⁻¹ with remarkable cycling stability.

Keywords: Li₄Ti₅O₁₂; TiNb₂O₇; composite; core-shell structure; full cell

1. Introduction

The substantial improvements in the efficiency of renewable energy sources, such as solar, wind, and hydroelectric power, have been instrumental in reducing greenhouse gas emissions and transitioning towards a net-zero carbon future. These clean energy sources are crucial for addressing climate change and reducing our dependence on fossil fuels. However, one of the challenges with renewable energy is its intermittent nature, which leads to fluctuating energy production. Energy storage technologies allow energy consumption to be separated in time from the production of energy, which can solve the variable and intermittent output of renewable energy sources. Lithium-ion batteries (LIBs) are currently the dominant storage system for portable electronics, electric vehicles, and large-scale plants to help electricity grids ensure a reliable supply of renewable energy. While graphite anodes, known for their large cell voltage, have been widely used in current commercial LIBs, their significant safety issues caused by the solid electrolyte interphase (SEI) film and dendritic lithium have restricted their widespread adoption in the next generation of LIBs [1,2].

Compared with the traditional graphite anode material, LTO is considered a highly promising anode material for LIBs [3–5] and hybrid electrochemical storage devices [6,7]. This is due to its remarkable characteristics, such as zero-strain behavior during Li^+ insertion/extraction processes, superior cycling stability, and high voltage plateau at around 1.55 V (Li^+/Li), leading to significant safety features. However, the LTOs still showed inherent low electronic conductivity, ionic diffusion coefficient, and theoretical capacity (175 mA h g^{-1}) [8–10], considerably restricting their rate performance. Numerous approaches, including surface modification [11–13], morphology control [14,15], and element doping [16,17], have been proposed to enhance the electrochemical kinetics of LTO anode materials. Nevertheless, the intrinsically low capacity of LTO remains its Achilles' heel. Compared to spinel LTO with a low capacity, TNO has a high theoretical capacity of 388 mA h g^{-1} due to multiple $\text{Ti}^{4+}/\text{Ti}^{3+}$ and $\text{Nb}^{5+}/\text{Nb}^{3+}$ redox couples [18,19]. Furthermore, TNO's working voltage of approximately 1.6 V is very close to that of LTO (1.55 V) [20,21]. Therefore, TNO is highly suitable for combining with LTO, enabling the development of an anode composite with high capacity, outstanding rate performance, long-lifespan, and excellent safety.

CS structures generally exhibit exceptional chemical and physical characteristics in comparison to their single-component counterparts and hence are extensively used in energy storage [22–24]. The energy storage materials with CS structure can provide few advantages such as (1) protect the core from outside environmental changes; (2) restrict volume expansion and (3) selectively percolate ions or molecules onto the core [25]. Various studies have been proposed to prepare CS structured materials, including techniques like layer-by-layer absorption [26], template-assisted method [27], in situ polymerization [28] and coaxial electrospray [29]. However, these methods are always a complicated, tedious and time-consuming process and have limitations that hinder the precise control of the composition, morphology, and interfacial properties of the CS composites. Conversely, spray-drying technology provides a straightforward and easily scalable method for producing particles. The foreign elements can be easily added in the synthesis process through the spray drying in a single step within a short time. In addition, the spray-dried method can efficiently produce the CS structured composites

using precursors with different particle sizes [30] or employing the two-fluid nozzle to atomize the slurry forming the CS structure [31].

In this study, we have developed the CS-structured TNO/LTO microspheres for the first time, resulting in a novel anode composite with remarkable rate capability and high capacity. To achieve this goal, we first synthesized highly conductive LTO (MCP-LTO_x) by co-doping with Cr³⁺/Mg²⁺, phosphidation, and modulation of oxygen vacancy. The resulting MCP-LTO_x demonstrates excellent rate performance attributed to the significant improvement in electrical conductivity. Then, the high-capacity TNO NPs prepared via the sol-gel route and the high-rate MCP-LTO_x were uniformly dispersed in the diluted poly(3,4-ethylenedioxythiophene) polystyrene sulfonate (PEDOT:PSS) solution. Lastly, the well-mixed suspension underwent further processing with a spray-dried method to produce the CS composite (CS-TNO@MCP-LTO_x) with TNO shell and MCP-LTO_x core. Our results indicate that the electric conductivity of MCP-LTO_x is much higher than that of TNO. In conventional blending, the TNO NPs tend to form aggregation within the binary composite. The higher insulating TNO aggregation within the active layer could pose an obstacle to charge transfer during the charge/discharge process. In contrast, the CS structure, the CS-TNO@MCP-LTO_x without TNO aggregation, exhibits a homogeneous distribution of conductivity, which can facilitate the charge transport. Consequently, the CS-TNO@MCP-LTO_x demonstrates enhanced rate performance and cycling stability compared to the conventional blended sample.

2. Experimental Section

2.1 Preparation of bare and MCP-LTO_x anode materials

This study prepared the LTO and modified LTO materials via the spray-dried method as follows. Initially, a combination of 411.34 g of TiO₂ powder, 155.2 g of Li₂CO₃, 11.34 g of Mg(CH₃COO)₂·4H₂O, 24.33 g of Cr(CH₃COO)₃·nH₂O, 14.91 g of NH₄H₂PO₄ and 60 mL of PVA solution (10%) was introduced to 1360 mL of deionized water. Subsequently, the mixture underwent mechanical mixing through the ball milling process to form a homogeneous suspension. The thoroughly mixed suspension was transferred into a spray dryer to generate the LTO precursor. Finally, the spray-

dried precursor was subsequently subjected to further heating in the N₂ atmosphere at 800°C for 2 hr, forming an MCP-LTO_x microsphere. The bare LTO microsphere was annealed in an air atmosphere without doping and surface modification. The bare and modified samples were labeled as LTO and MCP-LTO_x, respectively.

2.2 Preparation of TNO anode material

The TNO NPs were synthesized via the hydrothermal reaction. In a typical procedure, the tetrabutyl titanate (1.3 mL) and NbCl₅ (2.284 g) were added to 60 mL of ethanol with vigorous stirring for 1 hr. Then, the mixture was transferred into a hydrothermal reactor and heated at 180 °C for 72 hr to obtain the TNO precursor. Finally, the TNO precursor was washed with deionized water several times, dried, and annealed in an air atmosphere at 800 °C for 4 hr to produce TNO NPs.

2.3 Preparation of TNO/MCP-LTO_x CS composites

The as-prepared MCP-LTO_x and TNO were dispersed in deionized water with various content ratios. To enhance the adhesion and charge transfer between the MCP-LTO_x and TNO, the highly conductive PEDOT:PSS (Clevios PH1000) was added to the MCP-LTO_x and TNO mixture. Under intensely mechanical stirring, the well-mixed solution was pumped into the spray dryer for secondary granulation. During the spray-dried process, the TNO NPs can be uniformly covered on the MCP-LTO_x microsphere, forming the TNO and MCP-LTO_x CS composites. For comparison, the bare TNO/MCP-LTO_x composites were prepared by dispersed in deionized water with PEDOT:PSS, mechanically mixed, and dried at 80 °C to produce the blended composite. The traditionally blended and CS composites were labeled as TNO/MCP-LTO_x and CS-TNO@MCP-LTO_x, respectively.

3. Results and Discussion

In this study, we prepared highly conductive LTO by spray-drying method combined with ionic doping, phosphidation, and modulation of oxygen vacancy to improve its rate capability dramatically. The XRD patterns of the bare LTO and MCP-LTO_x, as shown in **Fig. 1a**, can be identified as pure spinel phase (JCPDS No. 26-1198) without obvious impurities such as non-reacted TiO₂ or other metal oxides derived from the Cr³⁺/Mg²⁺ doping. The results indicate the successful ionic doping and the well-

mixing of all precursors during the wet-grinding process. **Fig. 1b** displays the Raman spectra of bare LTO and MCP-LTO_x. The spectra of the two samples contain three main bands (230.6, 424.4, and 671.2 cm⁻¹), two minor bands (342.4 and 749.3 cm⁻¹), and a weak shoulder at 263 cm⁻¹, which is consistent with previous reports [32,33]. The three bands at 230.6, 424.4, and 671.2 cm⁻¹ are attributed to F_{2g}, E_g, and A_{1g} modes of cubic spinel LTO. Compared with the bare LTO, MCP-LTO_x shows a much weaker Raman intensity, suggesting its structural disruption due to foreign-ion doping [34]. **Fig. 1c** shows the UV/Vis spectra of the two samples, and the absorption edges of LTO and MCP-LTO_x are at 341 and 530 nm, respectively. The band gap energy (*E_g*) for the LTO can be determined from the plots of ($\alpha h\nu$)^{1/2} as a function of *hν* based on the Tauc equation [35], as shown in **Fig. 1d**. The obtained *E_g* of MCP-LTO_x (2.72 eV) is much smaller than that of bare LTO (3.83 eV), suggesting the successful of ionic doping. The N₂ physisorption isotherms were measured to evaluate the surface area of bare LTO and MCP-LTO_x. As shown in **Fig. S1**, the surface area values for the two samples are very similar (11.7 and 12.5 m² g⁻¹ for LTO and MCP-LTO_x). Besides, the particle size distribution of the two samples is shown in **Fig. S2**. The mean particle sizes (*D*₅₀) of LTO and MCP-LTO_x are 12.2 and 12.6 μm. These results indicate that the modification process cannot change the powder properties. In addition, the XPS analysis was also carried out to further investigate the effect of the modifications, including doping, phosphidation, and modulation of annealing conditions on the LTO properties. The XPS survey spectra of LTO and MCP-LTO_x are compared, as shown in **Fig. 1e**. It can be observed that the Cr³⁺/Mg²⁺ co-doped and phosphidated LTO reveals not only Li, Ti, and O signals but also three additional signals for Cr, Mg, and P, indicating the successful incorporation of the chemical additives. The high-resolution Ti_{2p} XPS spectra of MCP-LTO_x and LTO are displayed in **Fig. 1f** and **g**, respectively. The Ti 2p spectrum can be deconvoluted into Ti⁴⁺ and Ti³⁺ peaks, indicating the presence of mixed valence states. The Ti³⁺/Ti⁴⁺ ratio calculated based on the XPS area is around 0.204. In contrast, the LTO only shows a single valence state. It has been reported that the LTO annealed in the reducing or hypoxic atmosphere can cause the partial reduction of Ti⁴⁺ ions and the Mg²⁺ [36] and Cr³⁺ [37] doping in LTO can induce the partial reduction of Ti⁴⁺ to Ti³⁺ due to the higher electrovalence, which can significantly increase the

conductivity [38, 39]. The deconvoluted P_{2p} XPS spectrum of MCP-LTO_x is also presented in **Fig. 1h**, which contains CH-P, Ti-O-P, and Li-O-P bonding. The formation of Ti-O-P and Li-O-P glassy phases originating from the phosphidation can enhance the ionic transport of LTO, leading to better electrochemical performance [40, 41]. The high resolution Mg_{2p} and Cr_{2p} XPS spectra of MCP-LTO_x are also provided in **Fig. S3**.

The material characterizations of TNO anode material synthesized via the sol-gel route are shown in **Fig. 2**. All the XRD peaks of the sol-gel derived TNO, as shown in **Fig. 2a**, are observed to coincide with the monoclinic structure of standard TNO (JCPDS No. 77–1374) and the as-prepared TNO is free from impurity phases. The Raman and FTIR spectra of the TNO are presented in **Figs. 2b** and **2c**. The Raman bands at 999.3 and 886.4 cm^{-1} correspond to vibrations of the NbO_6 octahedra [42], and the other two bands at 641.5 and 532.9 cm^{-1} are ascribed to the metal–oxygen stretching of TiO_6 octahedra [43]. As shown in **Fig. 2c**, the FTIR band at 1633 cm^{-1} is caused by the vibration of hydroxyl groups from the physically absorbed moisture [44]. The stretching vibrations of the Nb-O bonds and the Nb-O-Nb bridging bonds can be attributed to the bands at 960 cm^{-1} and 507 cm^{-1} [45]. The bands observed at 855 and 703 cm^{-1} are originated from the Ti-O-Ti bonds [46]. These results clearly confirm that the monoclinic TNO has been successfully prepared. **Figs. 2d** and **2e** present the TEM images of the TNO to further study the morphology of the sol-gel-derived sample. It can be seen that the as-prepared TNO is composed of irregular particles with a particle size distribution ranging between 20 and 50 nm. In **Fig. 2e**, the high-resolution TEM image exhibits distinguishable lattice fringes with a lattice distance of 0.34 nm, corresponding to the d spacing of the (003) lattice planes in the monoclinic TNO structure [47]. The N_2 physisorption isotherm was measured to evaluate the surface area of the TNO. As shown in **Fig. 1c**, the TNO shows a typical type II isotherm, indicating its nonporous structure, and the surface area is found to be 30.4 $m^2 g^{-1}$.

The galvanostatic charge/discharge (GCD) curves of the LTO and MCP-LTO_x are compared, as shown in **Figs. 3a** and **3b**. The MCP-LTO_x demonstrates a clear advantage over bare LTO, exhibiting significantly improved rate capability and lower polarization. At a low current density of 17.5 $mA g^{-1}$,

both LTO and MCP-LTO_x deliver a capacity of approximately 169.5 mA h g⁻¹, closely approaching the theoretical value of 175 mA h g⁻¹. Nevertheless, at a high current density of 3500 mA g⁻¹, the MCP-LTO_x exhibits a significantly higher discharge capacity of 142.3 mA h g⁻¹ than the bare LTO, which only achieves 14.0 mA h g⁻¹. The improved rate capability of the MCP-LTO_x is undoubtedly attributed to the synergistic effect of ionic doping, surface modification, and modulation of oxygen vacancy. The GCD curves of the sol-gel derived TNO with different current densities ranging between 17.5 and 3500 mA g⁻¹ are also shown in **Fig. 3c**. A high discharge capacity of approximately 255.5 mA h g⁻¹ can be achieved for the TNO NPs at 17.5 mA g⁻¹. Unfortunately, it suffers from poor rate performance, and the discharge capacity at 3500 mA g⁻¹ is only 25.5 mA h g⁻¹. The rate capabilities of the LTO, MCP-LTO_x, and TNO are summarized in **Fig. 3d**. Clearly, MCP-LTO_x and TNO demonstrate complementary characteristics. MCP-LTO_x possesses excellent rate capability but limited specific capacity. On the other hand, TNO has a high capacity but inferior rate ability. Therefore, combining the two materials makes it possible to develop a composite material with high capacity and excellent rate capability.

The similar operating voltages of LTO and TNO allow the perfect integration of the two materials into a composite for high-performance anode materials. In this study, we utilized the micro-sized MCP-LTO_x and nano-sized TNO as components to prepare a CS composite via the spray-drying approach. As shown in **Fig. 4a**, we dispersed the MCP-LTO_x and TNO in water with diluted PEDOT:PSS as a conductive binder to form a stable suspension. After the spray-drying process, the CS composite with MCP-LTO_x core and TNO shell can be produced. The XRD patterns of the CS-TNO@MCP-LTO_x prepared with different weight ratios are presented in **Fig. 4b**. The diffraction peaks of the binary composite exhibit contributions from the two individual components without any impure peaks. As the weight ratio of TNO increases from 10% to 100%, there is a noticeable and significant increase in the intensity of the diffraction peaks of TNO. The electronic conductivity of the MCP-LTO_x and TNO can be directly measured by the 4-probe van der Pauw method [48]. As shown in **Fig. 4c**, the TNO is non-conductive, and the value cannot be measured due to its too low conductivity, which is out of the measurement limitation. In contrast, the electronic conductivity of MCP-LTO_x reaches a value as high

as $7.3 \times 10^{-9} \text{ S cm}^{-1}$, which results from the synergistic effect of the co-doping, phosphidation, and regulation of the annealing atmosphere. It is well known that the NPs always show a strong tendency to aggregate owing to the high surface energy [49, 50]. In the conventional blending process, the TNO/MCP-LTO_x composites can form severe phase separation with high-resistance TNO domain, as shown in **Fig. 4d**. In this situation, the charge would only pass the highly conductive MCP-LTO_x pathway and avoid the high-resistance TNO aggregation during the charging process. As a result, the non-uniform conductivity distribution within the anode electrode is unfavorable for the energy storage performance. In contrast, the CS-TNO@MCP-LTO_x can uniformize the conductivity of the composite film, as shown in **Fig. 4e**. Compared with the traditional blended film, the CS structured composite without the large TNO aggregation (high-resistance domain) can improve the charge transfer, which also can enhance the rate capability. Moreover, the unique structure with zero-strain LTO core and TNO shell can reduce the impact of volume change during repeated charge–discharge cycling leading to better dimensional stability.

The SEM morphologies of the CS-TNO@MCP-LTO_x composites with different content ratios are presented in Fig. 5. The SEM image (**Fig. 5a**) reveals that the sol-gel derived TNO NPs are rough spheroid in shape with a mean particle size of ~40 nm. As shown in Fig. 5b, the spray-dried MCP-LTO_x displays a micro-sized spherical morphology with a porous structure. The zoom-in SEM image of MCP-LTO_x, as shown in **Fig. 5c**, shows the porous surface composed of irregular polyhedral particles with a mean grain size of ~150 nm. With increasing the content ratio of TNO from 0 to 50 wt%, as shown in **Figs. 5c–f**, it can be observed that the CS-TNO@MCP-LTO_x surface exhibits a progressively increasing number of nanosized particles. These results indicate that the CS-TNO@MCP-LTO_x composites were successfully constructed.

To further confirm the CS structure, a CS-TNO@MCP-LTO_x with an open hole of approximately 400 nm on the microsphere shell was chosen for EDS elemental mapping, as shown in **Figs. 6a–b**. It can be seen that the Nb element homogeneous distributes on the microsphere surface except for the open hole (**Fig. 6c**), which proves the nonexistence of Nb element within the CS-TNO@MCP-LTO_x

microsphere. In contrast, the Ti element can be seen in the whole microsphere surface (Fig. 6d). Furthermore, **Fig. 6e** shows the element line scan analysis across the hole according to Fig. 6b. It displays the concentration distributions of Ti and Nb elements along the green line as shown in Fig. 6e. The element line scan analysis demonstrates that the Nb concentration is relatively lower on the breach region, which is consistent with the EDS mapping results. Furthermore, we utilized the FIB-SEM to acquire EDS mapping on the cross-section of the CS-TNO@MCP-LTO_x microsphere. The FIB-SEM image and the corresponding EDS mapping are shown in Fig. 6f. A carbon layer was applied to the CS-TNO@MCP-LTO_x before the FIB milling process to prevent the CS-TNO@MCP-LTO_x surface from ion beam irradiation damage. It can be clearly observed that the Nb element is uniformly distributed on the surface of the microsphere, indicating that the core shell structure has been successfully constructed. The corresponding TEM images of the CS-TNO@MCP-LTO_x microsphere are also shown in Fig. S4. In addition, the surface area of the CS composites with a TNO content of 10 wt%, 30 wt% and 50 wt% are found to be 14.7, 19.3 and 24.3 m² g⁻¹, respectively. The surface area is larger than that of pristine MCP-LTO_x (12.5 m² g⁻¹) but smaller than that of TNO (30.4 m² g⁻¹). The N₂ adsorption-desorption isotherms for the CS-TNO@MCP-LTO_x with different TNO contents are shown in Fig. S5.

The CV measurement was conducted on the blended TNO/MCP-LTO_x and CS-TNO@MCP-LTO_x composites to clarify the effects of the CS structure on their electrochemical property. The CV profiles of the pristine MCP-LTO_x and TNO stepped at 0.1 mV s⁻¹ are exhibited in **Figs. 7a–b**. The MCP-LTO_x shows a cathodic and anodic peak at 1.50 and 1.60 V, respectively, related to the Li-insertion/extraction process in MCP-LTO_x [51]. From the CV curve of TNO in **Fig. 7b**, the broad bulge between 1.0 and 1.4 V can be ascribed to the Nb⁴⁺/Nb³⁺ redox couple, the other two pair of redox peaks at 1.62 V/1.66 V and 1.75 V/1.96 V can be related to the valence variation of Nb⁵⁺/Nb⁴⁺ and Ti⁴⁺/Ti³⁺, respectively [52, 53]. For the CS-TNO@MCP-LTO_x composite (TNO=50 wt%), the CV profile clearly shows the characteristic peaks consisting of the features of MCP-LTO_x and TNO, indicating both the two components can show electrochemical response in the CS composite (**Fig. 7c**). The CV profiles of the blended and CS composites with various content ratios (TNO=10, 30 and 50 wt%) are presented in **Figs.**

7d–f and **Figs. 7h–j**, respectively. With increasing the scan rate, all samples' anodic and cathodic peaks shift to lower and higher voltages, respectively. However, the CS-TNO@MCP-LTO_x composites reveal a lower degree of distortion of CV profile than those of blended composites, indicating a smaller EP. The better electrochemical property of the CS composites is probably caused by the uniform conductivity without high-resistance TNO aggregation, resulting in lower internal resistance.

The GCD curves of the CS-TNO@MCP-LTO_x composites with different content ratios are shown in **Figs. 8a–c**. All the samples display a plateau at 1.55~1.6 V, which aligns with the operating potentials of LTO and TNO. With increasing the TNO content from 10 to 50 wt%, the slope of the discharge curve at 1.5–1.0 V gradually becomes smaller. The discharge capacity of the CS-TNO@MCP-LTO_x composites increased from 177.0 to 193.5 and 210.0 mA h g⁻¹ for the TNO contents, rising from 10 to 30 and 50 wt%, respectively. **Figs. 8d–e** compare the EP estimated from the voltage difference between charge and discharge plateaus. Notably, the EP of CS composites is always lower than those prepared by traditional blending, indicating a lower internal resistance. The rate capability of the two composites is also compared, as shown in **Figs. 8f–g**. Each CS composite exhibits a better rate performance than the corresponding blended composite due to the lower EP. The results clearly show that the construction of CS structure can improve the electrochemical kinetics of binary composite. The specific capacities of the CS-TNO@MCP-LTO_x with different TNO contents are summarized in Fig. 8h. It can be observed that all the CS-TNO@MCP-LTO_x composites have greater capacity values than that of bare LTO when the current density remains below 875 mA g⁻¹. However, the CS-TNO@MCP-LTO_x composite (TNO 50 wt%) exhibits a significant capacity reduction when the current density exceeds 875 mA g⁻¹, resulting in a lower value than bare LTO. Based on our experimental results, the optimal TNO content can be determined to be 30 wt%. The resulting composite can deliver larger capacities than the bare LTO across the entire range of C-rates. **Fig. 8i** shows the cycling stability of the TNO/MCP-LTO_x and CS-TNO@MCP-LTO_x composites (TNO 30 wt%) cycled at 1050 mA g⁻¹. The capacity of CS-TNO@MCP-LTO_x can be maintained at 151.7 mA h g⁻¹ with a retention of 91.8% after 300 cycles, while the blended TNO/MCO-LTO_x composite shows a faster capacity fading with a retention of only

87.2% (134.3 mA h g⁻¹). The improved cycling stability of CS-TNO@MCP-LTO_x may be ascribed to the unique CS structure without the TNO aggregation. In the designed structure, the zero-strain MCP-LTO_x core can stabilize the active layer, and the uniform TNO shell can weaken the mechanical strain of structural and volume changes [54].

The EIS measurement was also carried out to identify the origin of better electrochemical performance of the CS-TNO@MCP-LTO_x than TNO/MCP-LTO_x composite. As shown in **Fig. 9a**, the typical Nyquist plots of both samples are composed of a depressed semicircle followed by an inclined line. The Nyquist plot of CS-TNO@MCP-LTO_x shows a smaller semicircle than that of TNO/MCP-LTO_x, indicating its lower charge transfer resistance (R_{ct}). **Fig. 9b** shows the plot of Z_{re} versus $\omega^{-1/2}$. The slope (σ) obtained from the $Z_{re}-\omega^{-1/2}$ plot can be used to determine the Li⁺ ion diffusion coefficient (D_{Li}) according to the relation, $D_{Li}=R^2T^2/2A^2n^4F^4C^2\sigma^2$ [55]. The estimated D_{Li} value of CS-TNO@MCP-LTO_x is 1.86×10^{-11} cm²/s, 3.3 times larger than that of TNO/MCP-LTO_x 5.62×10^{-12} cm²/s. Furthermore, the dependences of the peak current (obtained from the CV curve) on the square root of the scan rate for the two samples are exhibited in **Fig. 9c**. It can be seen that the CS-TNO@MCP-LTO_x composite reveals a more significant slope than that of TNO/MCP-LTO_x, which also implies its faster kinetics based on the Randles-Sevcik equation [56]. The Nyquist plots of CS-TNO@MCP-LTO_x with different TNO contents are shown in **Fig. 9d**. As the high-resistance TNO content is increased from 10 to 30 and 50 wt%, the R_{ct} value exhibits a corresponding increase from 241.7 to 270.8 and 294.4 Ω , respectively. Typically, the resistance of a LIB electrode can be categorized into two components: material resistance and interface resistance between the active layer and the metal collector. Takeda et al. have conducted individual measurements of both material resistances of the active layer and the interface resistance between the active layer and the current collector by the electrode resistance meter (RM2610 HIOKI) [57–59]. In this study, the material and interface resistance of the two composite electrodes were also evaluated, as shown in **Figs. 9e** and **9f**, respectively. **Fig. 9e** shows a noticeable increase in the material resistance of the composite electrode as the TNO content rises due to the high resistance of TNO. Compared to the TNO/MCP-LTO_x electrodes, all the CS-TNO@MCP-LTO_x

electrodes exhibit a lower material resistance under the same TNO concentration, aligning with the findings from the EIS analysis. In contrast, the interface resistances for all the samples are almost unchanged (**Fig. 9f**), demonstrating that the active layer cannot alter the interface resistance.

Finally, we evaluate the practical application of the CS-TNO@MCP-LTO_x by using the CS-TNO@MCP-LTO_x anode and LNMO cathode to assemble the full LIBs (CS-TNO@MCP-LTO_x//LNMO). The CV curves of the LNMO cathode and CS-TNO@MCP-LTO_x (TNO=30 wt%) anode are shown in **Fig. 10a**. The LNMO cathode displays a high working potential of 4.59/4.83 V due to the Ni²⁺/Ni³⁺/Ni⁴⁺ redox couples. Based on their respective voltages, the pairing of CS-TNO@MCP-LTO_x anode and LNMO cathode can result in LIBs with a voltage of 3.16 V. During the formation process, the GCD curve of TNO@MCP-LTO_x//LNMO pouch cell with a designed capacity of 3.5 Ah is presented in **Fig. 10b**. The image of the pouch cell is shown in the inset of **Fig. 10b**. The pouch cell exhibits a voltage plateau around 3.12 V, which is following the CV findings while providing a capacity of 3.4 Ah that closely matches the designed value. The TNO@MCP-LTO_x//LNMO full cell achieves a remarkable energy density of 122.0 Wh kg⁻¹, surpassing the energy density of the MCP-LTO_x//LNMO cell (104.5 Wh kg⁻¹) by approximately 1.17 times. The formation curve of the LNMO//LTO full cell is shown in **Fig. S6**. The rate performance of the TNO@MCP-LTO_x//LNMO pouch cell is exhibited in **Fig. 10c**. The TNO@MCP-LTO_x//LNMO full cell can deliver a capacity of 3.37 Ah at a discharge rate of 0.7 A. Even at high current density of 21 A, the capacity of TNO@MCP-LTO_x//LNMO pouch cell still can remain 2.04 Ah with a capacity retention of 60.5%. The remarkable rate performance of the TNO@MCP-LTO_x//LNMO pouch cell can be ascribed to the synergistic effect of the modification of LTO and the construction of the CS composite. Fig. 10d shows the long-term cycling performance of the TNO@MCP-LTO_x//LNMO LIB at a rate of 10.5 A. After 400 cycles, TNO@MCP-LTO_x//LNMO full cell can still deliver a capacity of 2.22 Ah to reach 83.1% of the initial value, manifesting remarkable cycling stability.

4. Conclusion

We have successfully prepared the TNO and MCP-LTO_x composite with CS structure through a spray-dried approach. The CS-TNO@MCP-LTO_x with a homogeneous conductivity distribution can provide an unimpeded pathway for charge transport during the charge/discharge process. In contrast, the traditional TNO/MCP-LTO_x composites suffer from severe TNO aggregation caused by the high surface energy resulting from their nanoscale particle size. The TNO phase separation forms high-resistance domains within the active layer due to its low conductivity. Consequently, during the charge/discharge process, the charge tends to avoid these high-resistance TNO aggregations, resulting in inefficient utilization of the aggregated TNO and subsequently leading to poor energy storage performance. Benefited by the unique CS architecture, the CS-TNO@MCP-LTO_x reveals smaller EP and D_{Li} , enhancing the electrochemical kinetics at high charge/discharge rates. Meanwhile, the CS composites can also weaken the mechanical strain of structural and volume changes during Li⁺ insertion/extraction reaction, leading to better cycling stability. The present study demonstrates the feasibility of using TNO/MCP-LTO_x composites with CS structure as a high-performance anode electrode for high-power LIBs.

Acknowledgments

This study was supported by the National Science and Technology Council (MSTC) of Taiwan (grant nos. MOST 111-2628-E-011-003-MY2).

REFERENCES

- (1) C. Zhu, L. Sun, C. Chen, J. Tian, W. Shen, R. Xiong, Lithium-ion battery degradation diagnosis and state-of-health estimation with half cell electrode potential, *Electrochim. Acta* 459 (2023) 142588.
- (2) J. Liu, Y. Zhang, J. Bai, L. Zhou, Z. Wang, Influence of lithium plating on lithium-ion battery aging at high temperature, *Electrochim. Acta* 454 (2023) 142362.
- (3) T. Yuan, Z. Tan, C. Ma, J. Yang, Z. F. Ma, S. Zheng, Challenges of spinel $\text{Li}_4\text{Ti}_5\text{O}_{12}$ for lithium-ion battery industrial applications, *Adv. Energy Mater.* 7 (2017) 1601625.
- (4) Z. N. Ezhyeh, M. Khodaei, F. Torabi, Review on doping strategy in $\text{Li}_4\text{Ti}_5\text{O}_{12}$ as an anode material for Lithium-ion batteries, *Ceram. Int.* 49 (2023) 7105–7141.
- (5) Y. R. Kung, C. Y. Li, P. Hasin, C. H. Su, J. Y. Lin, Effects of butadiene sulfone as an electrolyte additive on the formation of solid electrolyte interphase in lithium-ion batteries based on $\text{Li}_4\text{Ti}_5\text{O}_{12}$ anode materials, *Polymers* 15 (2023) 1965.
- (6) C. Lv, W. He, J. Jiang, E. Zhen, H. Dou, X. Zhang, Structure optimization of solvent-free $\text{Li}_4\text{Ti}_5\text{O}_{12}$ electrodes by electrostatic spraying for lithium-ion capacitors, *J. Power Sources* 556 (2023) 232487.
- (7) Z. Ye, F. Zhong, Y. Chen, Z. Zou, C. Jiang, Unique CNTs-chained $\text{Li}_4\text{Ti}_5\text{O}_{12}$ nanoparticles as excellent high rate anode materials for Li-ion capacitors, *Ceram. Int.* 48 (2022) 20237–20244.
- (8) T. Acharya, A. D. Pathak, S. Pati, High-temperature electrochemical performance of lithium titanate ($\text{Li}_4\text{Ti}_5\text{O}_{12}$) anode material in secondary lithium-ion batteries, *J. Energy Storage* 67 (2023) 107529.
- (9) L. Xiong, X. Zeng, S. Zhou, D. Yin, Z. Chen, J. Yin, L. Bai, J. Zhu, C. Huang, Y. Zhou, L. Yang, Porous $\text{Li}_4\text{Ti}_5\text{O}_{12}$ -induced cathode electrolyte interphases enable sustainable single-crystalline NCM cathodes, *Appl. Surf. Sci.* 613 (2023) 156043.
- (10) Z. Huang, P. Luo, H. Zheng, Z. Lyu, Sulfur-doped graphene promoted $\text{Li}_4\text{Ti}_5\text{O}_{12}@\text{C}$ nanocrystals for lithium-ion batteries, *J. Alloys Compd.* 908 (2022) 164599.

- (11) I. S. Jang, S. H. Kang, Y. C. Kang, K. C. Roh, J. Chun, Facile synthesis of surface fluorinated- $\text{Li}_4\text{Ti}_5\text{O}_{12}$ /carbon nanotube nanocomposites for a high-rate capability anode of lithium-ion batteries, *Appl. Surf. Sci.* 605 (2022) 154710.
- (12) T. Zhu, C. Yu, Y. Wu, Y. Wang, $\text{Li}_{1.4}\text{Al}_{0.4}\text{Ti}_{1.6}(\text{PO}_4)_3$ -modified $\text{Li}_4\text{Ti}_5\text{O}_{12}$ anode for lithium-ion storage with enhanced rate and cycling performance, *ACS Sustainable Chem. Eng.* 11 (2023) 482–490.
- (13) E.-C. Cho, C.-W. Chang-Jian, J.-A. Chou, C.-L. Chung, P.-C. Ho, K.-C. Lee, J.-H. Huang, J.-H. Huang, Y.-S. Hsiao, MWCNT-embedded $\text{Li}_4\text{Ti}_5\text{O}_{12}$ microspheres interfacially modified with polyaniline as ternary composites for high-performance lithium ion battery anodes, *Ceram. Int.* 46 (2020), 6801.
- (14) X. Chen, J. Chen, X. Zhou, M. You, C. Zhang, W. Yue, Two-dimensional graphene-based $\text{Li}_4\text{Ti}_5\text{O}_{12}$ with hierarchical pore structure and large pseudocapacitive effect as high-rate and long-cycle anode material for lithium-ion batteries, *Electrochim. Acta* 405 (2022) 139814.
- (15) H. Yu, C. Huang, Y. Deng, B. Chen, D. Wu, S. Xu, Y. Zhang, H. Zhao, Preparation of $\text{Li}^+:\text{TiO}_2$ nanowires, $\text{Li}_4\text{Ti}_5\text{O}_{12}$ nanotubes, and a $\text{Li}_4\text{Ti}_5\text{O}_{12}$ nanotube/graphene composite by single-spinneret electrospinning for application in a lithium-ion battery, *CrystEngComm* 24 (2022) 7482–7492.
- (16) L. Li, W. Jiang, X. Hu, G. Yang, Enhancing the rate performances of $\text{Li}_4\text{Ti}_5\text{O}_{12}$ by Mo^{4+} doping and MoO_2 -Mo dispersed on the surface, *J. Alloys Compd.* 933 (2023) 167406.
- (17) A. Lakshmi-Narayana, M. Dhananjaya, C. M. Julien, S. W. Joo, C. V. Ramana, Enhanced electrochemical performance of rare-earth metal-ion-doped nanocrystalline $\text{Li}_4\text{Ti}_5\text{O}_{12}$ electrodes in high-power Li-ion batteries, *ACS Appl. Mater. Interfaces* 15 (2023) 20925–20945.
- (18) S. Gong, Y. Wang, Q. Zhu, M. Li, Y. Wen, H. Wang, J. Qiu, B. Xu, High-rate lithium storage performance of TiNb_2O_7 anode due to single-crystal structure coupling with Cr^{3+} -doping, *J. Power Sources* 564 (2023) 232672.
- (19) G. Zhu, W. Jiao, Q. Li, Y. Zha, X. Liu, R. Che, Conductivity optimization via intertwined CNTs between $\text{TiNb}_2\text{O}_7@\text{C}$ microspheres for a superior performance Li-ion battery anode, *J. Colloid Interface Sci.* 607 (2022) 1103-1108.

- (20) S. Gong, Y. Wang, P. Zhang, M. Li, Y. Wen, J. Qiu, B. Xu, H. Wang, Self-assembly TiNb_2O_7 @MXene anode material for fast and stable lithium storage, *Energy Fuels* 37 (2023) 3159–3165.
- (21) N. V. Kosova, D. Z. Tsydpylov, Effect of mechanical activation and carbon coating on the electrochemistry of TiNb_2O_7 anodes for lithium-ion batteries, *Batteries* 8 (2022) 52.
- (22) C. Yang, X. Wang, Y. Ren, S. Gu, Q. Wang, H. Li, K. Yue, T. Gao, G. Zhou, $\text{NiFe}_2\text{V}_2\text{O}_8$ @N-Doped carbon Yolk-Double shell spheres for efficient lithium storage, *Chem. Eng. J.* 454 (2023) 140045.
- (23) C. Yang, X. Li, T. Gao, S. Gu, X. Wang, Y. Wang, Q. Wang, B. Sun, Y. He, G. Zhou, Novel quadruple-shelled hollow $\text{Zn}_{0.5}\text{Mn}_{0.5}\text{Co}_2\text{O}_4$ /RGO heterostructure enable rapid and stable lithium storage performance, *Chem. Eng. J.* 474 (2023) 145818.
- (24) Y. Ren, X. Li, Y. Wang, Q. Gong, S. Gu, T. Gao, X. Sun, G. Zhou, Self-template formation of porous yolk-shell structure Mo-doped NiCo_2O_4 toward enhanced lithium storage performance as anode material, *J. Mater. Sci. Technol.* 102 (2022) 186-194.
- (25) L. Su, Y. Jing, Z. Zhou, Li ion battery materials with core-shell nanostructures, *Nanoscale* 3 (2011) 3967-3983.
- (26) D. B. Shenoy, A. A. Antipov, G. B. Sukhorukov, H. Möhwald, Layer-by-layer engineering of biocompatible, decomposable core-shell structures, *Biomacromolecules* 4 (2003) 265–272.
- (27) B. Chen, N. Zhao, L. Guo, F. He, C. Shi, C. He, J. Li, E. Liu, Facile synthesis of 3D few-layered MoS_2 coated TiO_2 nanosheet core-shell nanostructures for stable and high-performance lithium-ion batteries, *Nanoscale* 7 (2015) 12895-12905.
- (28) R. Liu, D. Li, C. Wang, N. Li, Q. Li, X. Lü, J. S. Spendelow, G. Wu, Core-shell structured hollow SnO_2 -polypyrrole nanocomposite anodes with enhanced cyclic performance for lithium-ion batteries, *Nano Energy* 6 (2014) 73-81.
- (29) Y. H. Lee, F. Mei, M. Y. Bai, S. Zhao, D. R. Chen, Release profile characteristics of biodegradable-polymer-coated drug particles fabricated by dual-capillary electrospray, *J. Controlled Release* 145 (2010) 58–65.

- (30) I. Muhammad, M. Jabeen, P. Wang, Y. S. He, X. Z. Liao, Z. F. Ma, Spray-dried assembly of 3D N,P-Co-doped graphene microspheres embedded with core-shell CoP/MoP@C nanoparticles for enhanced lithium-ion storage, *Dalton Trans.* 50 (2021) 4555–4566.
- (31) N. Saadatkah, M. G. Rigamonti, D. C. Boffito, H. Li, G. S. Patience, Spray dried SiO₂ WO₃/TiO₂ and SiO₂ vanadium pyrophosphate core-shell catalysts, *Powder Technol.* 316 (2017) 434-440.
- (32) P. Dhaiveegan, H. T. Peng, M. Michalska, Y. Xiao, J. Y. Lin, C. K. Hsieh, Investigation of carbon coating approach on electrochemical performance of Li₄Ti₅O₁₂/C composite anodes for high-rate lithium-ion batteries, *J. Solid State Electrochem.* 22 (2018)1851–1861.
- (33) C. Zhu, J. Liu, X. Yu, Y. Zhang, Y. Zhang, X. Jiang, S. Wang, Q. Wang, P. Dong, Enhance the electrochemical performance of Li₄Ti₅O₁₂ with Co doping via a facile mechanical activation strategy, *J. Mater. Sci.: Mater. Electron.* 30 (2019) 5866–5873.
- (34) Y. R. Jhan, J. G. Duh, Electrochemical performance and low discharge cut-off voltage behavior of ruthenium doped Li₄Ti₅O₁₂ with improved energy density. *Electrochim. Acta* 63 (2012) 9-15.
- (35) Z. Wang, H. Guo, D. Ning, X. Ma, L. Zheng, D. Smirnov, K. Sun, D. Chen, L. Sun, X. Liu, Tuning fermi level and band gap in Li₄Ti₅O₁₂ by doping and vacancy for ultrafast Li⁺ insertion/extraction, *J. Am. Ceram. Soc.* 104 (2021) 5934-5945.
- (36) W. Wang, B. Jiang, W. Xiong, Z. Wang, S. Jiao, A nanoparticle Mg-doped Li₄Ti₅O₁₂ for high rate lithium-ion batteries, *Electrochim. Acta* 114 (2013) 198– 204.
- (37) H. Zou, X. Liang, X. Feng, H. Xiang, Chromium-modified Li₄Ti₅O₁₂ with a synergistic effect of bulk doping, surface coating, and size reducing, *ACS Appl. Mater. Interfaces* 8 (2016) 21407–21416.
- (38) Z. Yao, H. Yin, L. Zhou, G. Pan, Y. Wang, X. Xia, J. Wu, X. Wang, J. Tu, Ti³⁺ self-doped Li₄Ti₅O₁₂ anchored on N-doped carbon nanofiber arrays for ultrafast lithium-ion storage, *Small* 15 (2019) 1905296.
- (39) B. Ali, R. Muhammad, M. Islam, D. A. Anang, D. S. Han, I. Moez, K. Y. Chung, M. K. Cho, J. Y. Kim, M. G. Kim, K. W. Nam, Cd-doped Li_{4-x}Cd_xTi₅O₁₂ (x = 0.20) as a high rate capable and stable anode material for lithium-ion batteries, *ACS Appl. Energy Mater.* 6 (2023) 4198–4210.

- (40) M. R. Jo, K. M. Nam, Y. Lee, K. Song, J. T. Park, Y. M. Kang, Phosphidation of $\text{Li}_4\text{Ti}_5\text{O}_{12}$ nanoparticles and their electrochemical and biocompatible superiority for lithium rechargeable batteries, *Chem. Commun.* 47 (2011) 11474–11476.
- (41) K. S. Park, A. Benayad, D. J. Kang, S. G. Doo, Nitridation-driven conductive $\text{Li}_4\text{Ti}_5\text{O}_{12}$ for lithium ion batteries, *J. Am. Chem. Soc.* 130 (2008) 14930–14931.
- (42) S. Jia, Q. Zhou, F. Li, Y. Hu, C. Wang, X. Wang, S. He, X. Li, L. Li, T. Cui, High-pressure bandgap engineering and amorphization in TiNb_2O_7 single crystals, *CrystEngComm* 24 (2022) 2660–2666.
- (43) R. Qian, M. Yao, F. Xiao, T. Yao, H. Lu, Y. Liu, J. W. Shi, Y. Cheng, H. Wang, Polyvinylpyrrolidone regulated synthesis of mesoporous titanium niobium oxide as high-performance anode for lithium-ion batteries, *J. Colloid Interface Sci.* 610 (2022) 385–394.
- (44) A. V. Rao, R. R. Kalesh, G. M. Pajonk, Hydrophobicity and physical properties of TEOS based silica aerogels using phenyltriethoxysilane as a synthesis component, *J. Mater. Sci.* 38 (2003) 4407–4413.
- (45) S. Lou, Y. Ma, X. Cheng, J. Gao, Y. Gao, P. Zuo, C. Du, G. Yin, Facile synthesis of nanostructured TiNb_2O_7 anode materials with superior performance for high-rate lithium ion batteries, *Chem. Commun.* 51 (2015) 17293–17296.
- (46) S. Lou, X. Cheng, Y. Zhao, A. Lushington, J. Gao, Q. Li, P. Zuo, B. Wang, Y. Gao, Y. Ma, C. Du, G. Yin, X. Sun, Superior performance of ordered macroporous TiNb_2O_7 anodes for lithium ion batteries: Understanding from the structural and pseudocapacitive insights on achieving high rate capability, *Nano Energy* 34 (2017) 15–25.
- (47) H. Park, H. B. Wu, T. Song, X. W. Lou, U. Paik, Porosity-controlled TiNb_2O_7 microspheres with partial nitridation as a practical negative electrode for high-power lithium-ion batteries, *Adv. Energy Mater.* 5 (2015) 1401945.
- (48) H. Song, T. G. Jeong, Y. H. Moon, H. H. Chun, K. Y. Chung, H. S. Kim, B. W. Cho, Y. T. Kim, Stabilization of oxygen-deficient structure for conducting $\text{Li}_4\text{Ti}_5\text{O}_{12-\delta}$ by molybdenum doping in a reducing atmosphere, *Sci. Rep.* 4 (2014) 4350.

- (49) S. Shrestha, B. Wang, P. Dutta, Nanoparticle processing: Understanding and controlling aggregation, *Adv. Colloid Interface Sci.* 279 (2020) 102162.
- (50) M. A. Ashraf, W. Peng, Y. Zare, K. Y. Rhee, Effects of size and aggregation/agglomeration of nanoparticles on the interfacial/interphase properties and tensile strength of polymer nanocomposites, *Nanoscale Res. Lett.* 13 (2018) 214.
- (51) L. Zou, L. Gan, W. Song, C. Rong, L. Yang, L. Yu, Z. Ma, S. Lian, Improving electrochemical properties of $\text{Li}_4\text{Ti}_5\text{O}_{12}/\text{TiO}_2$ diphasic anode materials via Co-Cl co-doping, *J. Alloys Compd.* 960 (2023) 170765.
- (52) R. Muruganantham, M. C. Lin, P. K. Wang, B. K. Chang, W. R. Liu, Highly effective Al-doped titanium niobate porous anode material for rechargeable high-rate Li-ion storage performance, *J. Taiwan Inst. Chem. Eng.* 131 (2022) 104187.
- (53) Y. Sui, J. Guo, Z. Li, F. Jiang, X. Xia, H. Geng, Q. Liu, B. Wei, X. Zuo, Kinetics modulation of titanium niobium oxide via hierarchical MXene coating for high-rate and high-energy density lithium-ion half/full batteries, *Appl. Surf. Sci.* 576 (2022) 151890.
- (54) W. Lu, X. Guo, Y. Luo, Q. Li, R. Zhu, H. Pang, Core-shell materials for advanced batteries, *Chem. Eng. J.* 355 (2019) 208–237.
- (55) G. Zha, N. Hu, Y. Luo, F. Wang, R. Wu, Y. Li, H. Fu, X. Fu, Reducing Ni/Li disorder and boosting electrochemical performance of $\text{LiNi}_{0.8}\text{Co}_{0.067}\text{Fe}_{0.033}\text{Mn}_{0.1}\text{O}_2$ cathode material, *J. Taiwan Inst. Chem. Eng.* 144 (2023) 104730.
- (56) J. M. Park, S. H. Baek, W. I. Kim, S. J. Lee, G. S. Gung, H. S. Park, Hierarchical hybrid architecture of carbon nanotube branches grown onto steam activated-reduced graphene oxide/Ni nanoparticle for lithium-sulfur battery cathode, *Electrochim. Acta* 462 (2023) 142750.
- (57) A. Takeda, T. Nakamura, H. Yokouchi, H. Tomozawa, Resistance reduction effect by SDX® in lithium-ion batteries, *ECS Trans.* 80 (2017) 283–290.
- (58) Y. Arai, M. Kunisawa, T. Yamaguchi, H. Yokouchi, A. Matsuo, M. Ohmori, Studies of SDXTM on the boundary resistance between aluminum current collectors and cathode active material layers, *ECS Trans.* 50 (2013) 153–160.

- (59) A. Takeda, T. Nakamura, H. Yokouchi, H. Tomozawa, The mechanism of decreasing resistance by SDXTM in lithium ion battery, ECS Trans. 75 (2017) 17–25.

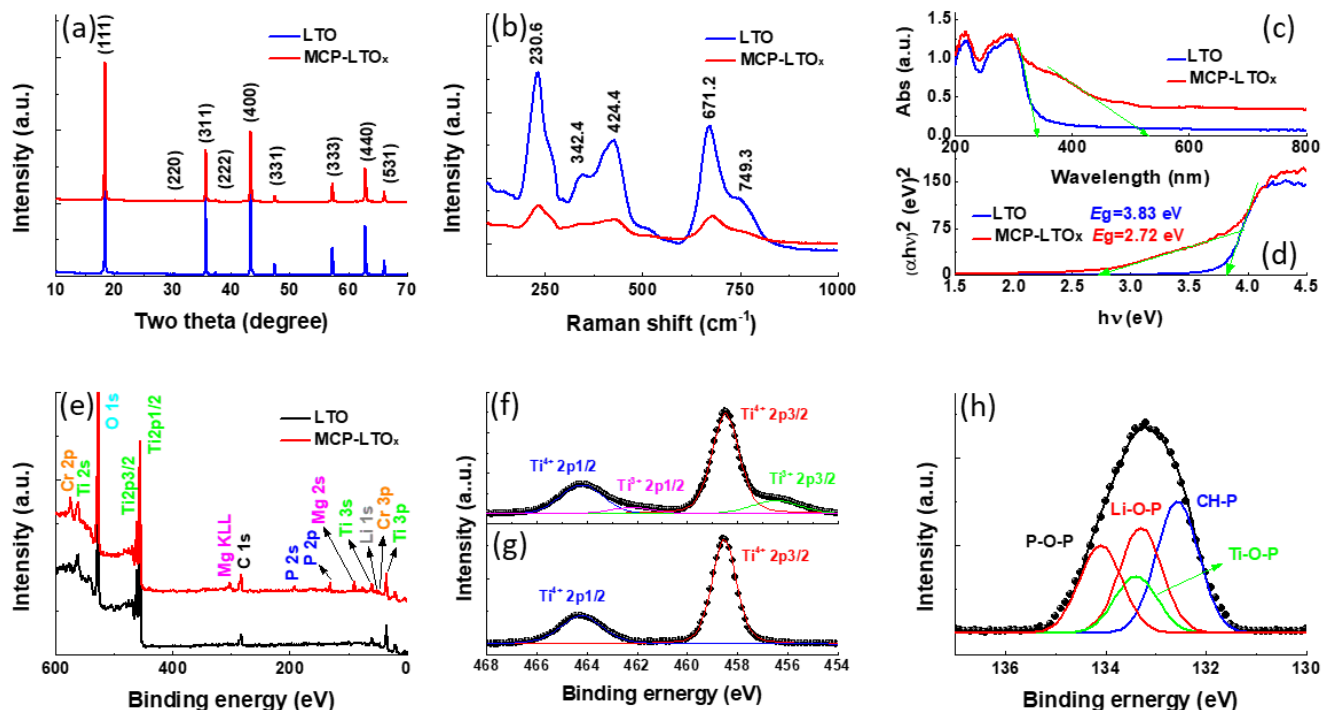


Figure. 1 Characterization of LTO and MCP-LTO_x. (a) XRD patterns; (b) Raman spectra; (c) UV/Vis spectra; (d) Tauc plots; (e) XPS survey; high-resolution Ti_{2p} XPS spectrum of (f) MCP-LTO_x and (g) LTO and (h) deconvoluted P_{2p} XPS spectrum of MCP-LTO_x.

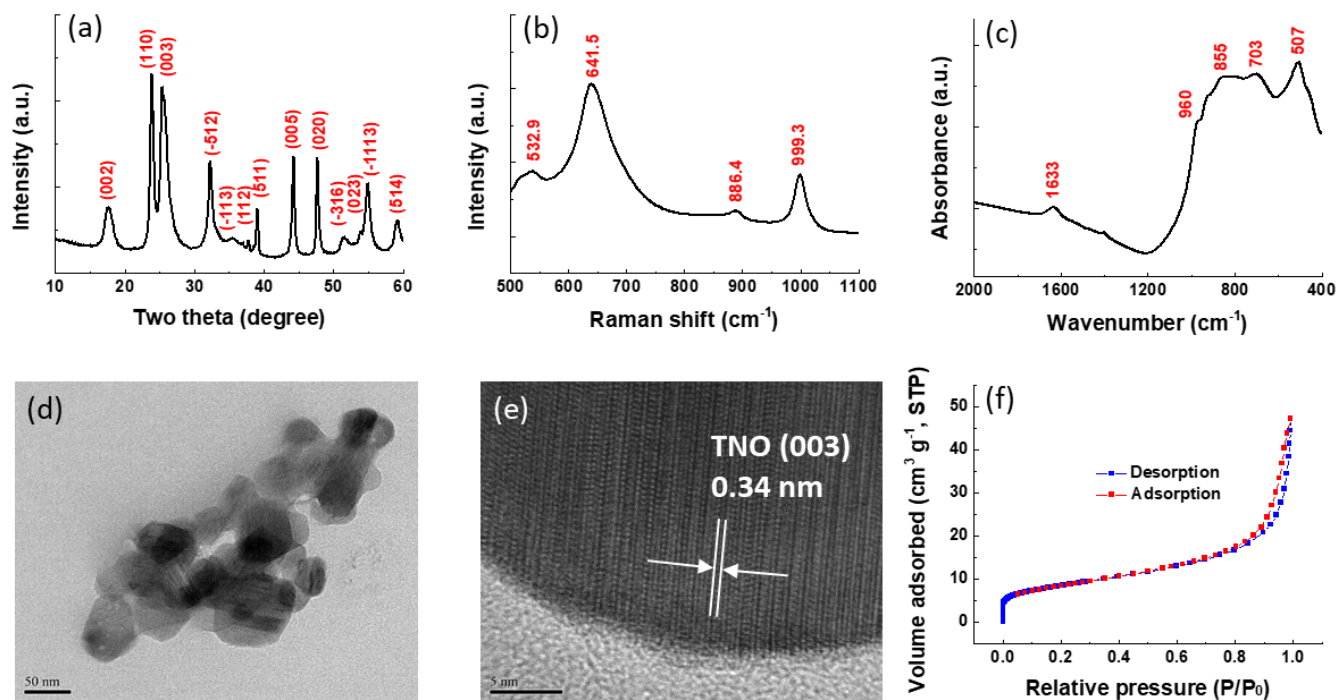


Figure 2. Characterizations of sol-gel derived TNO. (a) XRD pattern; (b) Raman spectrum; (c) FTIR spectrum; (d, e) TEM images; and (f) N₂ physisorption isotherm of the TNO NPs.

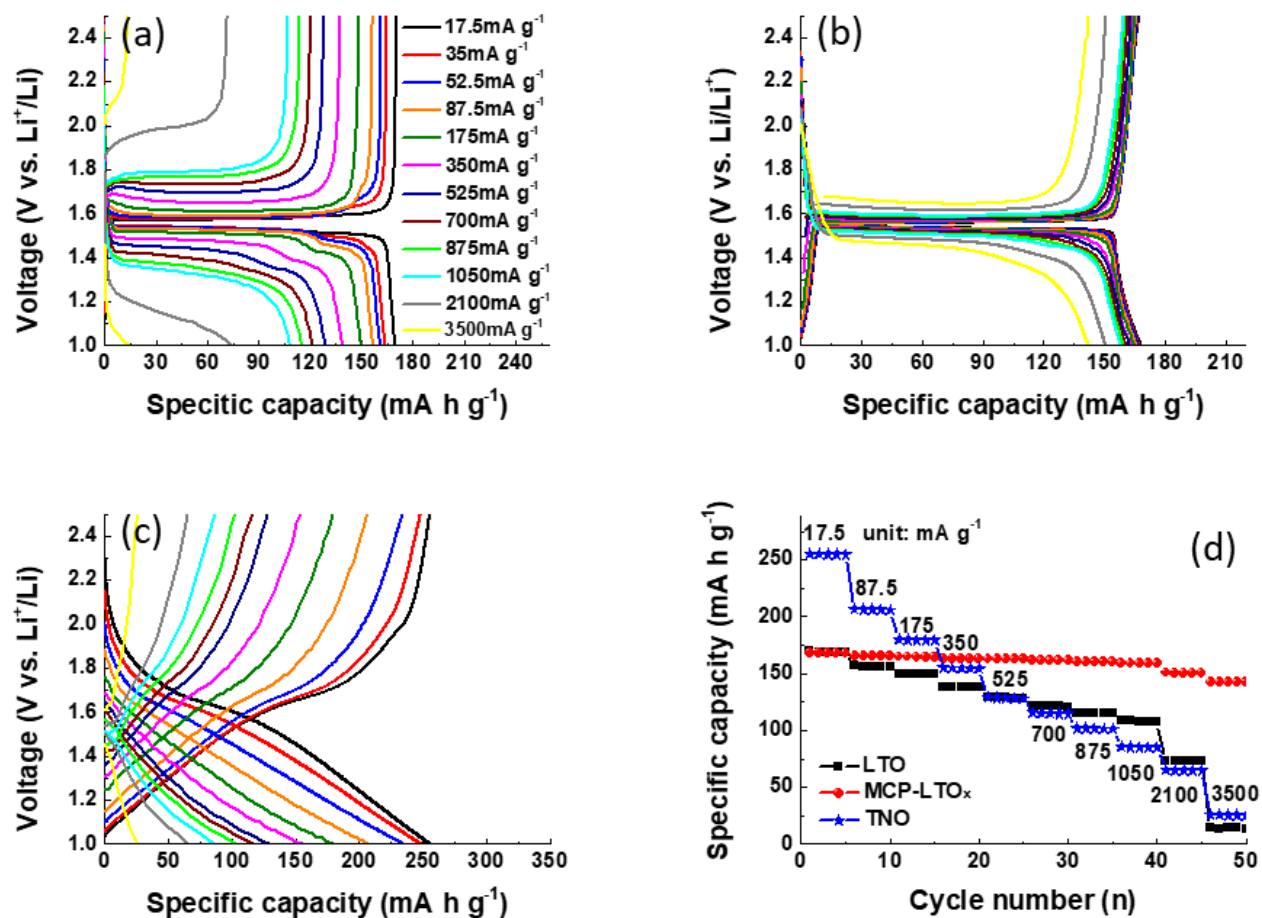


Figure 3. The energy storage performance of the LTO, MCP-LTO_x, and TNO. The GCD curves of (a) LTO, (b) MCP-LTO_x, and (c) TNO, and (d) the rate performance of LTO, MCP-LTO_x, and TNO.

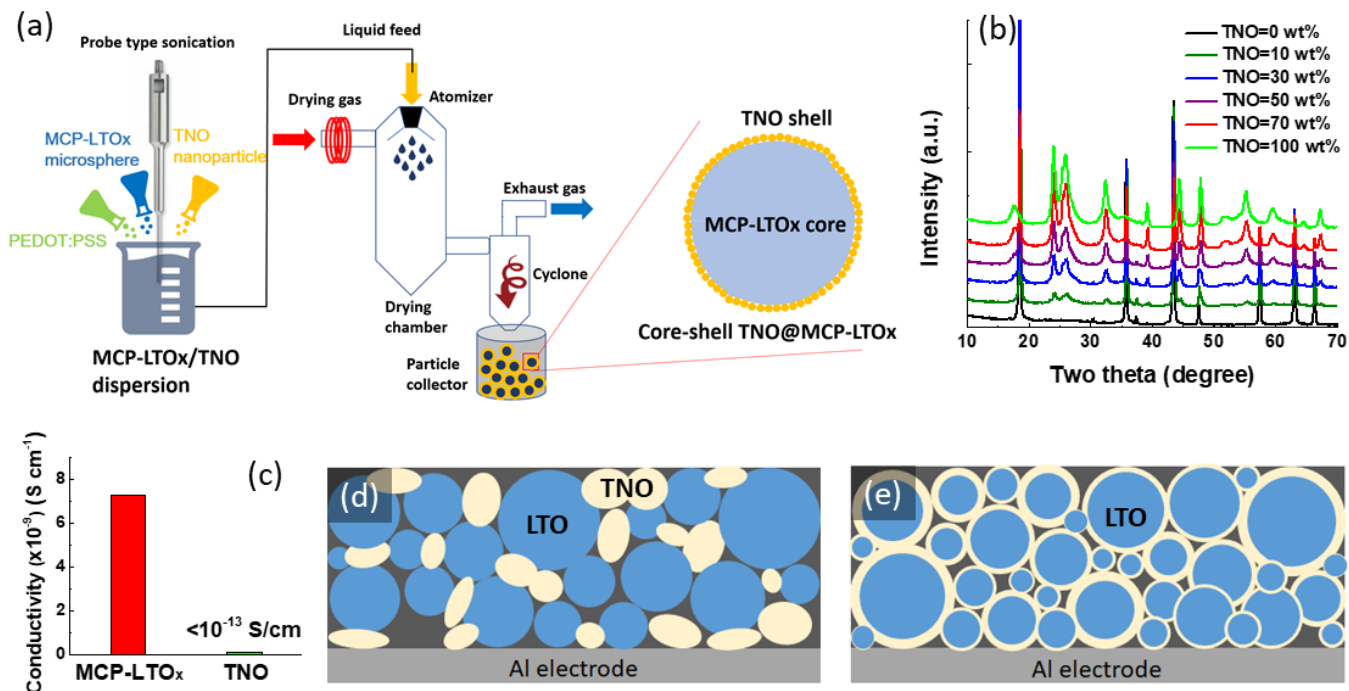


Figure 4. The preparation of CS-TNO@MCP-LTO_x composites. (a) Schematic illustration of the preparation of CS-TNO@MCP-LTO_x composite using PEDOT:PSS as a conductive binder; (b) the XRD patterns of CS-TNO@MCP-LTO_x composite with different TNO contents; (c) the conductivity of MCP-LTO_x and TNO; (d) schematic illustration of internal morphology of the TNO/MCP-LTO_x and CS-TNO@MCP-LTO_x electrodes.

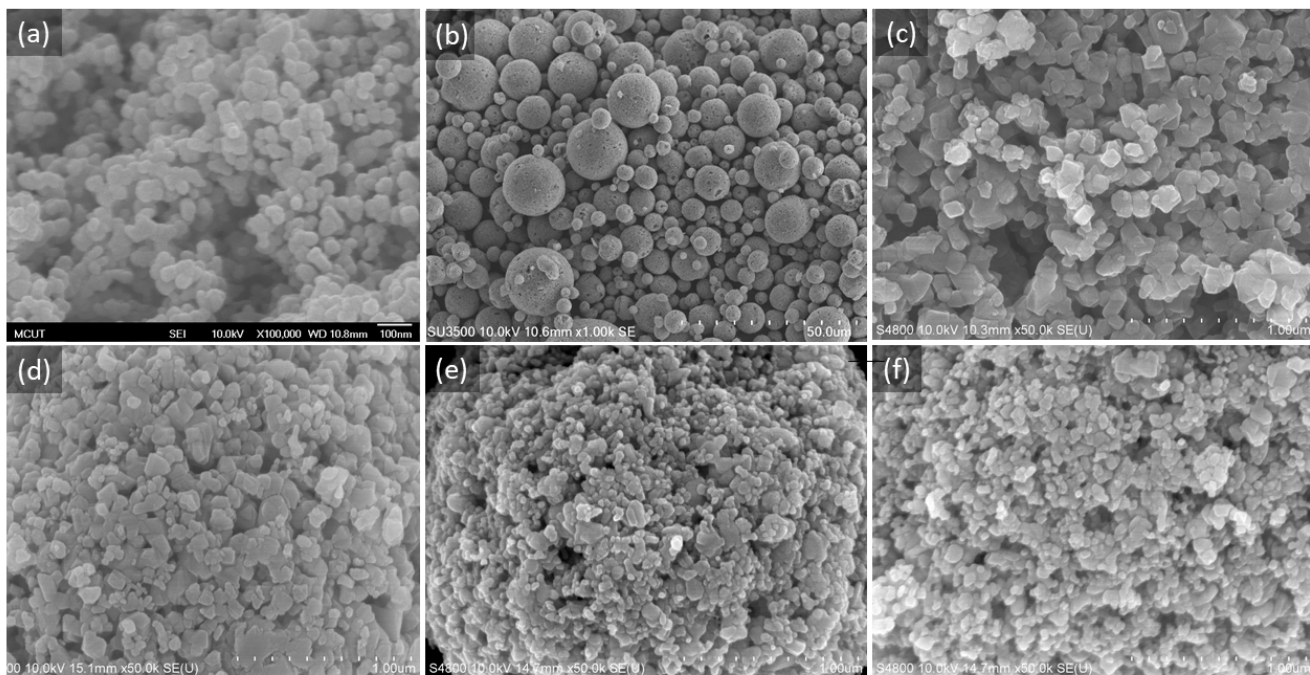


Figure 5. Surface morphology of CS-TNO@MCP-LTO_x composites. SEM images of (a) TNO NPs; (b, c) MCP-LTO_x; (d) CS-TNO@MCP-LTO_x (TNO=10 wt%); (e) CS-TNO@MCP-LTO_x (TNO=30 wt%) and (f) CS-TNO@MCP-LTO_x (TNO=50 wt%).

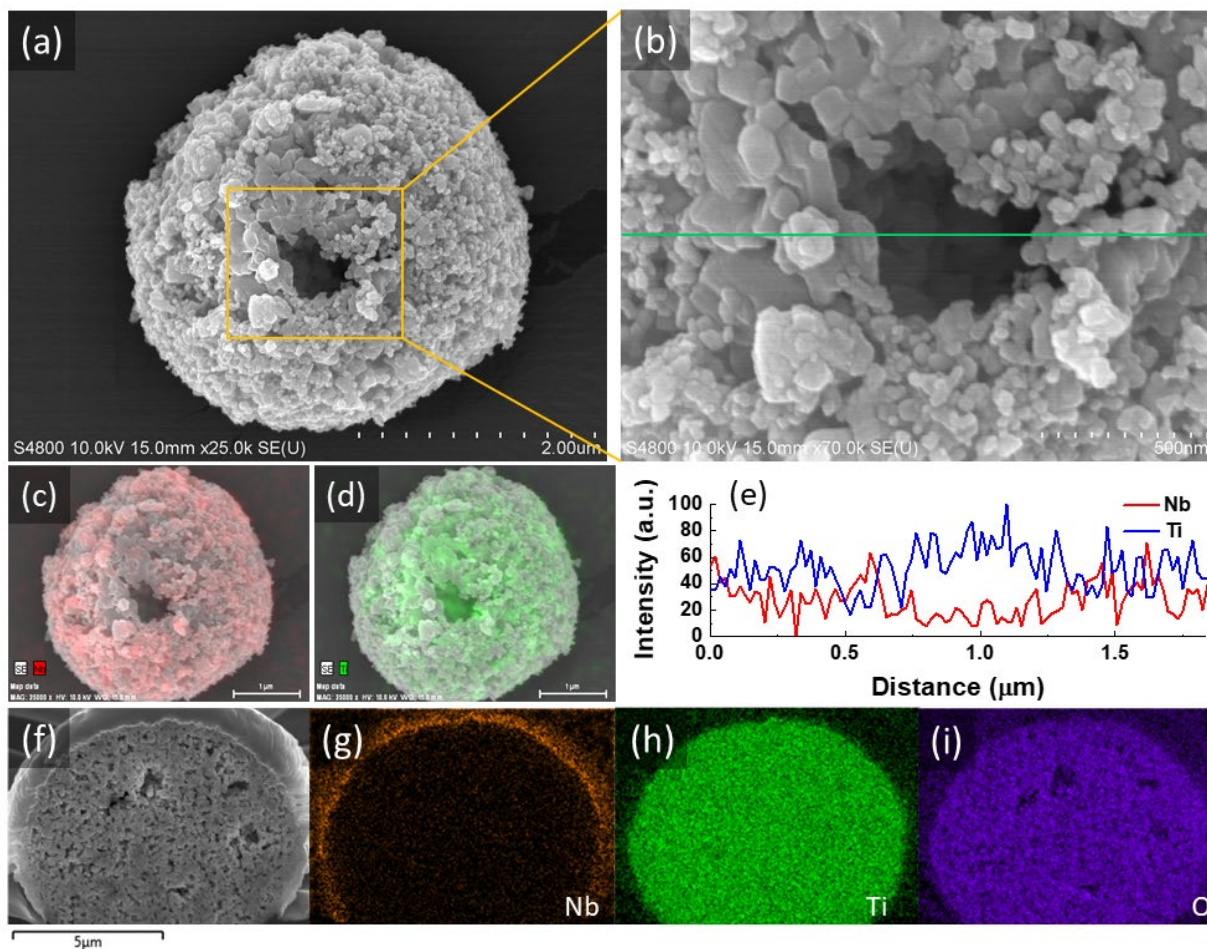


Figure 6. SEM-EDS analysis of CS-TNO@MCP-LTO_x composite. (a, b) SEM images of CS-TNO@MCP-LTO_x with an open hole of approximately 400 nm were chosen for EDS elemental mapping; EDS mapping of (c) Nb and (d) Ti elements; (e) element line scan analysis across the hole according to **Fig. 6b**. (f) The cross-sectional FIB-SEM image of CS-TNO@MCP-LTO_x microsphere; the EDS mapping of (g) Nb element; (h) Ti element and (i) O element.

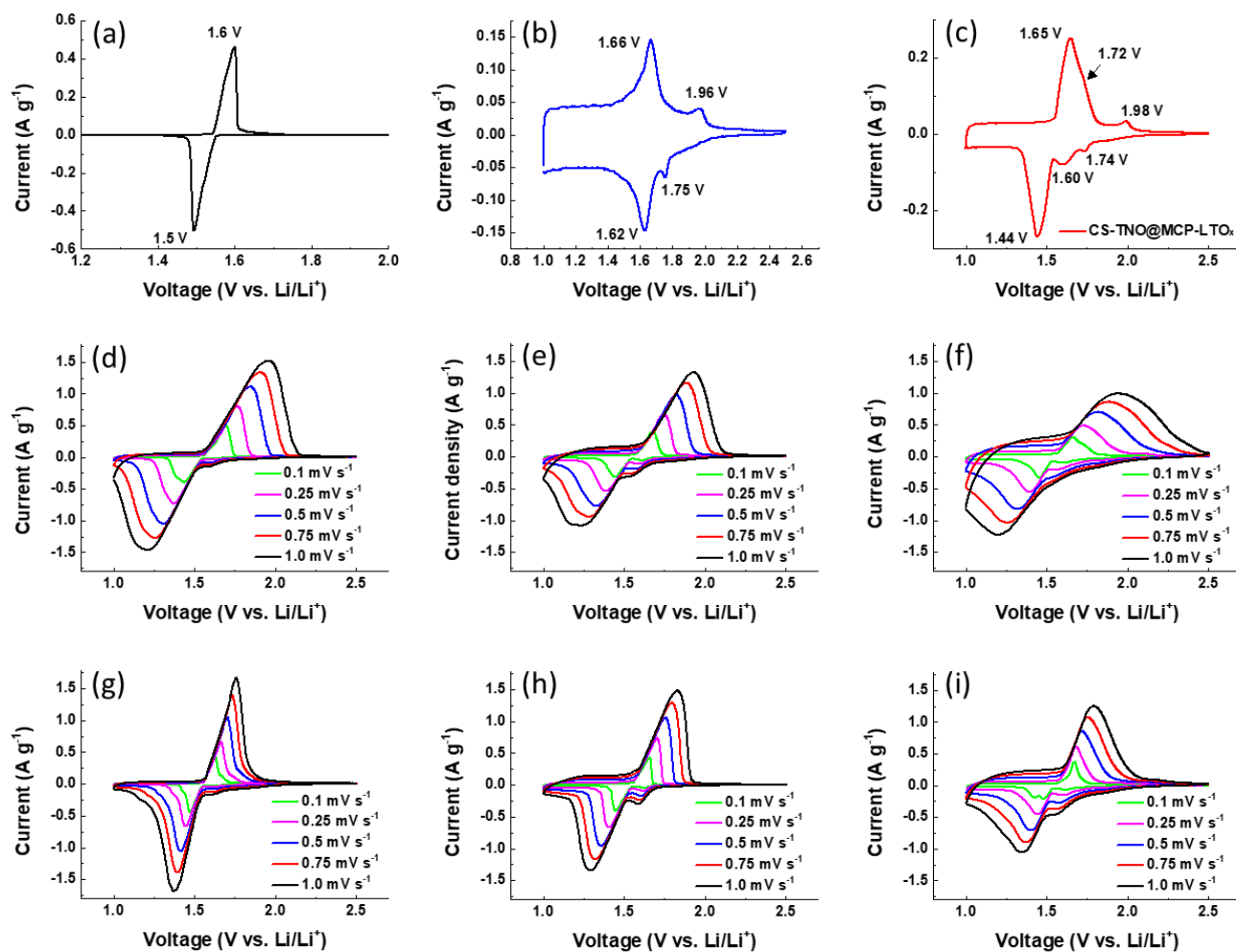


Figure 7. Electrochemical performance of CS-TNO@MCP-LTO_x composites. CV curves of (a) MCP-LTO_x; (b) TNO; (c) CS-TNO@MCP-LTO_x stepped at 0.1 mV s⁻¹; CV curves of the blended TNO/MCP-LTO_x composites with TNO content of (d) 10 wt%; (e) 30 wt%; (f) 50 wt% and CS-TNO@MCP-LTO_x with TNO content of (g) 10 wt%; (h) 30 wt%; (i) 50 wt%.

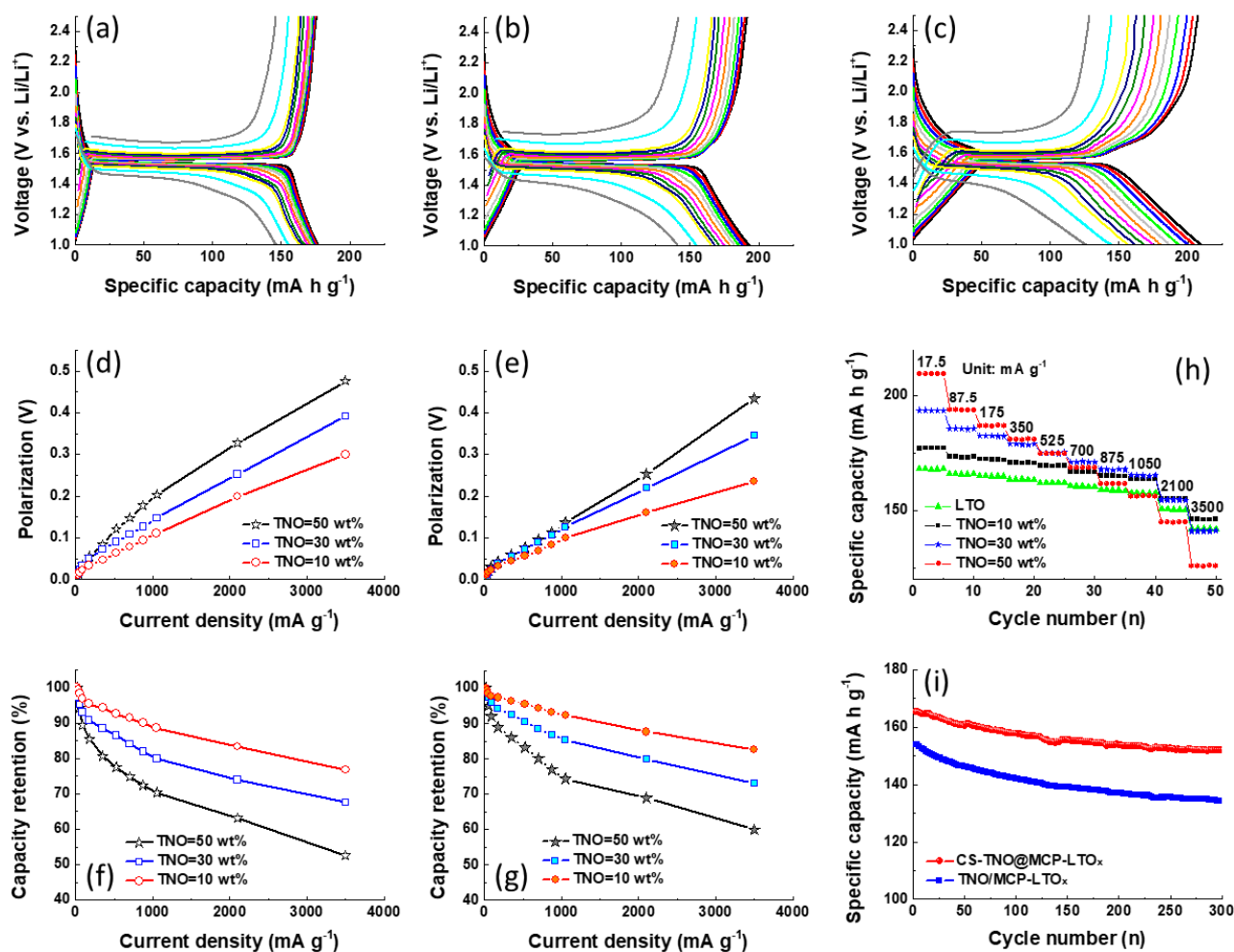


Figure 8. Comparison of energy storage for blended and CS composites. GCD curves of CS-TNO@MCP-LTO_x composites with different TNO contents (a) 10 wt%; (b) 30 wt%; (c) 50 wt%; EP estimated from the GCD curves for (d) TNO/MCP-LTO_x and (e) CS-TNO@MCP-LTO_x; rate performance of (f) TNO/MCP-LTO_x and (g) CS-TNO@MCP-LTO_x; (h) specific capacity of CS-TNO@MCP-LTO_x with different TNO contents and (i) cycling stability of TNO/MCP-LTO_x and CS-TNO@MCP-LTO_x composites.

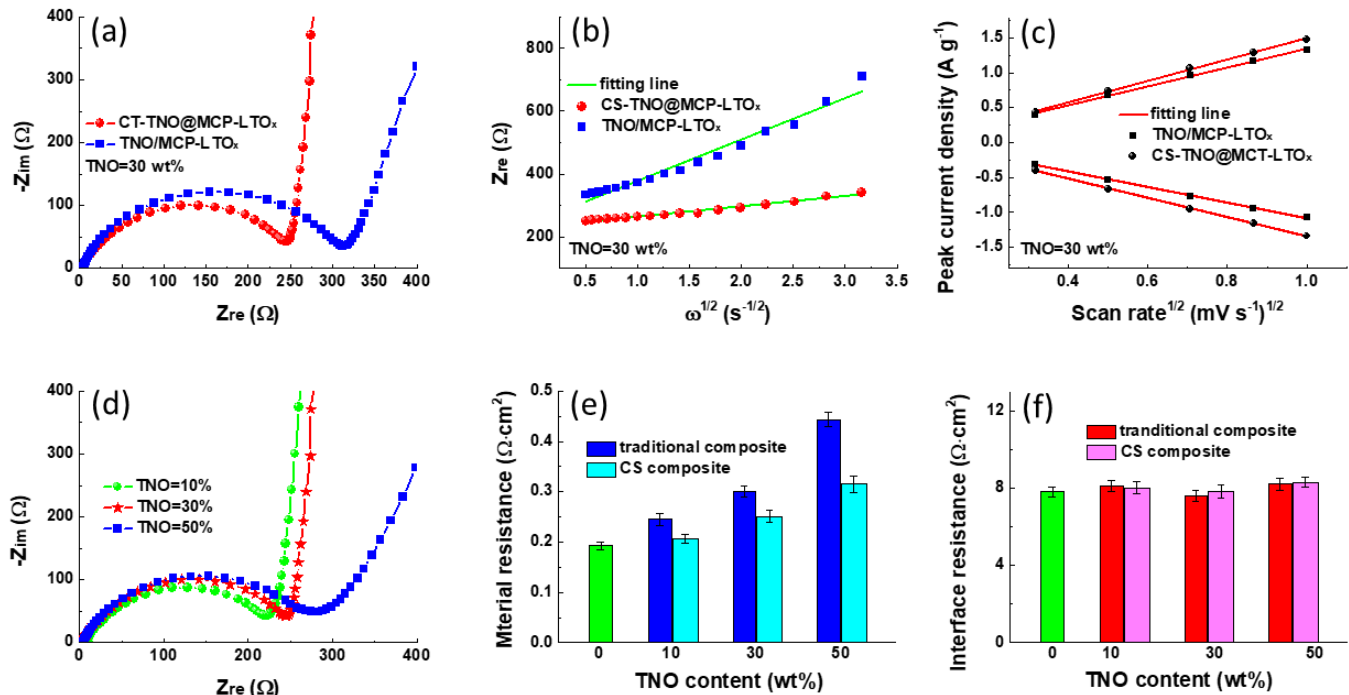


Figure 9. Electrochemical kinetics of CS-TNO@MCP-LTO_x composite. (a) Nyquist plots of the TNO/MCP-LTO_x and CS-TNO@MCP-LTO_x composites with a TNO content of 30 wt%; and (b) corresponding plots of real parts of complex impedance versus $\omega^{-1/2}$; (c) linear relationships between anodic and cathodic peak current densities and the square root of scan rate; (d) Nyquist plots of CS-TNO@MCP-LTO_x composites with various TNO contents; (e) effect of TNO content on material resistance and (f) effect of TNO content on the interface resistance.

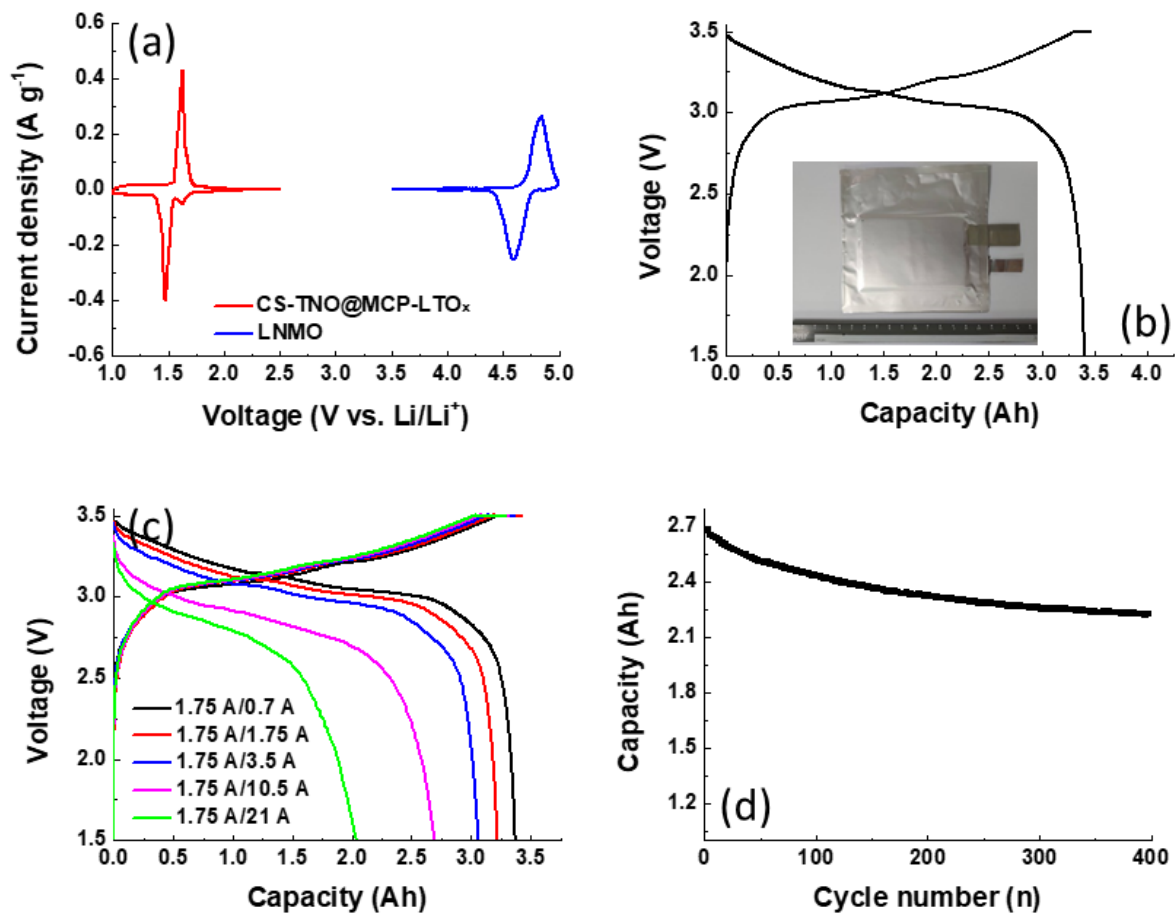


Figure 10. Electrochemical performance of CS-TNO@MCP-LTO_x//LNMO full LIB. (a) CV curves of CS-TNO@MCP-LTO_x (TNO=30 wt%) and LNMO; (b) GCD curve of TNO@MCP-LTO_x//LNMO pouch cell during the formation process (The insert shows the photograph of the pouch cell); (c) GCD curves of TNO@MCP-LTO_x//LNMO LIB with various C-rates and (d) cycling stability of the TNO@MCP-LTO_x//LNMO LIB.